

This is an Open Access document downloaded from ORCA, Cardiff University's institutional repository: <https://orca.cardiff.ac.uk/id/eprint/149966/>

This is the author's version of a work that was submitted to / accepted for publication.

Citation for final published version:

Aikman, Brech, Bonsignore, Riccardo, Woods, Ben, Doellerer, Daniel, Scotti, Riccardo, Schmidt, Claudia, Heidecker, Alexandra A., Pöthig, Alexander, Sayers, Edward J., Jones, Arwyn T. and Casini, Angela 2022. Highly-fluorescent BODIPY-functionalised metallacages as drug delivery systems: synthesis, characterisation and cellular accumulation studies. *Dalton Transactions* 51 (19), pp. 7476-7490. 10.1039/D2DT00337F

Publishers page: <http://dx.doi.org/10.1039/D2DT00337F>

Please note:

Changes made as a result of publishing processes such as copy-editing, formatting and page numbers may not be reflected in this version. For the definitive version of this publication, please refer to the published source. You are advised to consult the publisher's version if you wish to cite this paper.

This version is being made available in accordance with publisher policies. See <http://orca.cf.ac.uk/policies.html> for usage policies. Copyright and moral rights for publications made available in ORCA are retained by the copyright holders.



Highly-Fluorescent BODIPY-functionalised Metallacages as Drug Delivery Systems: Synthesis, Characterisation and Cellular Accumulation Studies

Brech Aikman,^{a,†} Riccardo Bonsignore,^{a,b,†} Ben Woods,^c Daniel Doellerer,^d Riccardo Scotti,^a Claudia Schmidt,^a Alexandra A. Heidecker,^e Alexander Pöthig,^e Edward J. Sayers,^f Arwyn T. Jones^{f,*} and Angela Casini^{a,g,*}

With the aim of designing new metallocsupramolecular architectures for drug delivery, research has focused on porous 3-dimensional (3D)-metallacages able to encapsulate cytotoxic agents protecting them from metabolism while targeting them to cancer sites. Here, two self-assembled [Pd₂L₄]⁴⁺ cages (**CG1** and **CG2**) featuring 3,5-bis(3-ethynylpyridine)phenyl ligands (L) *exo*-functionalised with dipyrromethene (BODIPY) groups have been synthesised and characterised by different methods, including NMR spectroscopy and mass spectrometry. ¹H NMR spectroscopy studies shows that the cages are able to encapsulate the anticancer drug cisplatin in their hydrophobic cavity, as evidenced by electrostatic potential (ESP) analysis based on XRD studies. The stability of the cages in aqueous environment, and in the presence of the intracellular reducing agent glutathione, has been confirmed by UV-Visible absorption spectroscopy. The luminescence properties of the cages enabled the investigation of their cellular uptake and intracellular localisation in human cancer cells by confocal laser scanning microscopy. In melanoma A375 cells, cage **CG1** is taken up via active transport and endocytic trafficking studies show little evidence of transport through the early endosome while the cages accumulated in melanosomes rather than lysosomes. The antiproliferative activity of the lead cage was investigated in A375 together with two breast cancer cell lines, SK-BR-3 and MCF7. While the cage *per se* is non-cytotoxic, very different antiproliferative effects with respect to free cisplatin were evidenced for the [(cisplatin)₂⊂**CG1**.BF₄]⁺ complex in the various cell lines, which correlate with its different intracellular localisation profiles. The obtained preliminary results provide a new hypothesis on how the subcellular localisation of the cage affects the cisplatin intracellular release.

Introduction

The design of metal-based supramolecular systems has resulted in the construction of a myriad of fascinating structures with

highly diverse properties and potential applications in various fields, including catalysis, biology and medicine.¹ In this area, two main types of self-assembled supramolecules have been described, namely Metal Organic Frameworks (MOFs) and Supramolecular Coordination Complexes (SCCs). While MOFs are porous polymers formed by coordination bonds between metal ions or clusters and organic linkers,^{2,3} SCCs are well defined and discrete two- (2D) or three-dimensional (3D) structures.⁴ The latter have recently attracted great interest as either new therapeutic and/or imaging agents as well as novel drug delivery systems.^{5–10} Thus, various metal-based precursors have been used to synthesise SCCs of different shapes, including triangles, squares, helicates, rectangles, prisms, cubes and cages among others. Interestingly, the possibility to modify the ligand structure both pre- and post-self-assembly, via the covalent linkage of different functionalities to the SCC's architecture, is crucial for the development of innovative cancer *theranostics*;¹¹ e.g., enabling prolonged blood circulation, targeted drug release, accurate bioimaging, and superior anticancer performance. Despite these attractive features, the use of SCCs for biomedical applications is still in its infancy.

Within this framework, 3D-metallacages of general formula [M_xL_y]ⁿ (M = metal, L = ligand, n = charge) featuring an internal cavity and that have intrinsically low toxicity in cancerous and

^a Chair of Medicinal and Bioinorganic chemistry, Department of Chemistry, Technical University of Munich, Lichtenbergstr. 4, 85748 Garching b. München, Germany.

^b Dipartimento di Scienze e Tecnologie Biologiche, Chimiche e Farmaceutiche, Università degli Studi di Palermo, Viale delle Scienze, Edificio 17, 90128 Palermo, Italy.

^c Institute of Structural and Molecular Biology and Department of Biological Sciences, School of Science, Birkbeck University of London, Malet Street, London WC1E 7HX, United Kingdom.

^d Stratingh Institute for Chemistry, University of Groningen, Nijenborgh 4, 9747 AG, Groningen, The Netherlands.

^e Catalysis Research Center & Department of Chemistry, Chair of Inorganic and Metal-Organic Chemistry, Technical University of Munich, Ernst-Otto-Fischer Str. 1, D-85748 Garching b. München, Germany.

^f School of Pharmacy and Pharmaceutical Sciences, Cardiff University, CF10 3NB Cardiff, Wales, United Kingdom.

^g Munich Data Science Institute, Technical University of Munich, D-85748 Garching b. München, Germany

[†] Co-shared first authorship.

Electronic Supplementary Information (ESI) available: [NMR and MS spectra, fluorescence microscopy images, crystallographic data and electrostatic potential analysis. Time-lapse movie of live cells microscopy]. See DOI: 10.1039/x0xx00000x

non-tumorigenic cells, hold promise as drug delivery systems since small drug molecules can be encapsulated in their porous structure and protected from metabolism. Drug encapsulation is driven by non-covalent interactions within the host cavity (e.g. H-bonding, van der Waals interactions) as well as by hydrophobic effects which can kinetically and thermodynamically favour guest binding over water encapsulation.^{12,13}

Based on previous work by Fujita and coworkers,¹⁴ and within the M_2L_4 cage family, Crowley *et al.* designed a cationic $[Pd_2L_4]^{4+}$ cage using 2,6-bis(pyridin-3-ylethynyl)pyridine as the bidentate ligand, and characterised it by various methods, including 1H NMR spectroscopy, mass spectrometry and X-ray diffraction (XRD).¹⁵ Interestingly, the encapsulation of the anticancer drug cisplatin within the metallacage cavity was demonstrated by XRD studies, revealing that two molecules of the metallodrug could occupy the cavity, lined with the nitrogen atom from the central pyridine of the ligand.¹⁵ Unfortunately, while the cisplatin-cage host-guest complex formed in acetonitrile and DMF solutions, no host-guest interactions could be observed in more hydrogen bond-competitive solvents (water and DMSO).¹⁶

More recently, we explored similar cationic $[Pd_2L_4]^{4+}$ systems featuring bis(pyridyl) ligands, of general scaffold 3,5-bis(3-ethynylpyridine)phenyl, for the encapsulation of cisplatin¹⁷ and developed the *exo*-functionalisation of the ligands to add different active components, including fluorescent tags facilitating the study of the cellular accumulation of these systems by fluorescence microscopy,^{18,19} as well as tumor targeting peptides.^{20,21} Noteworthy, $[Pd_2L_4]^{4+}$ cages tethered to a blood brain barrier (BBB)-translocating peptide were synthesised by a combination of solid phase peptide synthesis and self-assembly procedures.²² Biodistribution studies of the cage, encapsulating radioactive pertechnetate - $[[^{99m}TcO_4]^- \subset \text{cage}]$ - in mice models demonstrated its brain penetration capability *in vivo*.²² It should be noted that, at variance with the aforementioned Pd^{2+} cages by Crowley *et al.*,¹⁵ the cavity of our $[Pd_2L_4]^{4+}$ cages is more hydrophobic, and therefore, cisplatin encapsulation is likely to be favoured over occupancy of the cavity by water molecules or other polar solvents.¹³ This hypothesis is corroborated by the enhanced cytotoxicity observed for $[\text{cisplatin} \subset \text{cage}]$ complexes vs free cisplatin *in vitro*.^{17,21,23} Notably, most of the reported metallacages and their precursors in our series were non-toxic in healthy rat liver tissue *ex vivo*,¹⁷ making them suitable for application as drug delivery systems.

In order to trace metallacages' cellular accumulation and sub-cellular distribution *in vitro*, we *exo*-functionalised 3,5-bis(3-ethynylpyridine)phenyl ligands with highly emissive boron dipyrromethene (BODIPY) moieties.²⁴ BODIPYs have already been successfully conjugated to different types of SCCs for fluorescence imaging and as photosensitisers for photodynamic therapy (PDT).^{25–28} Our preliminary results enabled visualisation of the cages in human cancer cells by fluorescence microscopy, highlighting uptake via an active transport mechanisms and accumulation in cytoplasmic vesicles.²⁴ To gain more insights into these systems and how their cellular accumulation

pathways may affect their drug delivery capability, we further refined the BODIPY- $[Pd_2L_4]^{4+}$ cage complex to enhance its stability in physiological conditions and overall photophysical properties. Therefore, two novel BODIPY *exo*-functionalised cages have been synthesised (Figure 1) with an improved stability profile and partly addressing the solubility limitations in biologically relevant medium. Noteworthy, simple modifications of the linker tethering the fluorophore to the cage scaffold via amide bond formation were sufficient to modulate the metallacages' properties. The new cages have been characterized by different methods, and the solid-state structure of the non-functionalized $[Pd_2L_4]^{4+}$ scaffold has been obtained by XRD. Further analysis of the hydrophobic character of the metallacage's cavity was performed by evaluation of its electrostatic potential.

Moreover, the encapsulation of cisplatin has been studied by NMR spectroscopy, and the ability of selected cages to enhance its antiproliferative effects in human cancer cells has been investigated *in vitro*. Fluorescence microscopy studies in fixed and live cells were performed on a selected BODIPY- $[Pd_2L_4]^{4+}$ cage, enabling investigation of its active uptake and sub-cellular distribution properties in human melanoma A375 cells. Interestingly, following cell uptake, the cages accumulate in intracellular vesicles attributable to melanosomes. Cell uptake was energy dependant confirming delivery to this organelle via endocytosis. Preliminary immunolabeling results utilising endo-lysosomal markers show that the cage is unlikely to have trafficked through conventional EEA1 positive early endosomes in A375 cells and subsequently did not accumulate in lysosomes. The intracellular distribution studies were further extended to other types of cancer cells, namely human breast cancer lines, SK-BR-3 and MCF7. Interestingly, very different sub-cellular localisation profiles were evidenced in these cell lines for the $[(\text{cisplatin})_2 \subset \text{CG1.BF}_4]$ complex, correlating with its different antiproliferative effects with respect to free cisplatin *in vitro*.

Results and discussion

Synthesis and characterisation

The synthesis of highly luminescent $[Pd_2L_4]^{4+}$ metallacages was achieved by the conjugation of the BODIPY fluorophore to the bispyridyl ligand scaffold *via* amide bond formation (Figure 1). The carboxylic and the benzylic acid-functionalised ligands (**L1** and **L2** in the supplementary material, Scheme S1) were synthesised according to a previously reported procedure,²⁹ and used for coupling to the BODIPY scaffold (**G1**) forming cage precursor **LG1** and **LG2**, respectively (Figure 1). Finally, the *exo*-functionalised BODIPY- $[Pd_2L_4]^{4+}$ metallacages were formed via self-assembly by mixing 4 equiv. of ligand with 2 equiv. of the Pd^{2+} precursor to achieve cage **CG1.X** ($X = BF_4^-$, NO_3^-) and **CG2.BF₄**, respectively. The ligands and cages have been characterised by NMR spectroscopy and electrospray ionization mass spectrometry (ESI-MS) (Figures S1-S16 in the supplementary material).

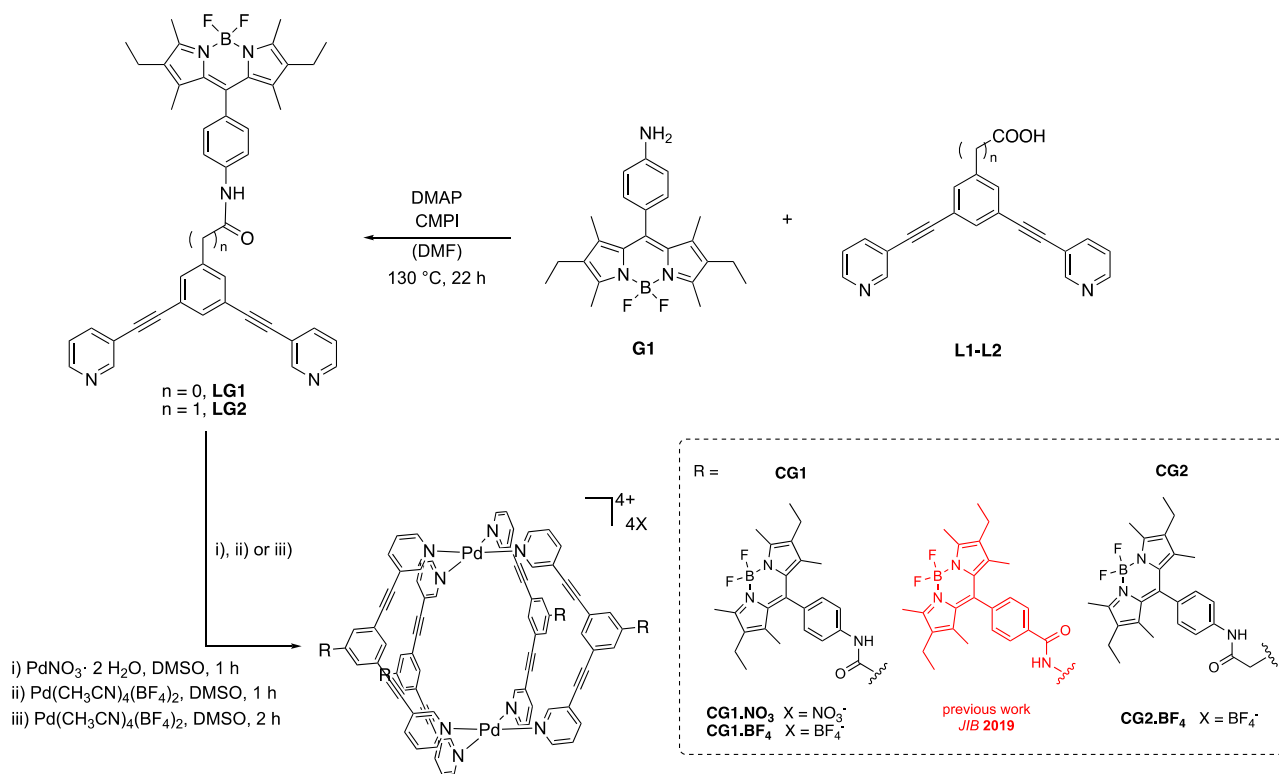


Figure 1 – Synthesis of *exo*-functionalized BODIPY-[Pd₂L₄]⁴⁺ metallacages reported in this study and related cage system investigated in previous work.²⁴

X-ray diffraction and electrostatic potential analysis

Crystals of the non-functionalized dipalladium Pd₂L₄-type cage with ligand **L2** were obtained by the vapour diffusion method as described in the experimental section. Suitable single crystals were evaluated by XRD and the compound was determined to crystallise in the monoclinic space group *C* 2/*m*. PLATON/SQUEEZE procedure was applied to account for diffuse electron density, which could not be refined explicitly (see Experimental for details). Based on visual inspection of the residual electron density map before solvent masking, we assume that no electron density corresponding to an anion was affected (for details see ESI, Figures F+G). The molecular structure of the cage shows similar features as previously reported for [M₂L₂]⁴⁺ cages (Figure 2A).^{17,19} The four bidentate ligands **L2** are coordinated in a square-planar fashion to two Pd²⁺ ions each with a Pd-Pd distance of 11.874 Å. The coordination geometry of the Pd²⁺ ions deviates slightly from square-planarity with angles of 90.06(15), 89.92(9), 90.09(15) and 89.92(11)° and Pd-N distances of 2.027(3) and 2.028(3) Å.

The average pore size of the cage amounts to 8.38 Å and the pore is limited by the hydrogen atoms of distal pyridine and equatorial phenyl units of **L2** (for details see SI). Closer inspection of the crystal structure reveals an intriguing linear packing along the *a*-axis (Fig. S17 in SI). Hereby, the *exo*-carboxylic/carboxylate groups apparently form a linear coordination between two functional groups of neighbouring cages. Although no hydrogens could be located at the –COO⁻ groups, the linear cage arrangement strongly points towards

hydrogen bonding and therefore, suggests the (partial) presence of hydrogens i.e. –COOH groups in the *exo*-functionalised Pd₂L₄ cage. This is supported by inspection of the charge balance, since three tetrafluoroborate anions were found per cage in the solid state (as opposed to zero BF₄⁻ necessary in case of four anionic (carboxylate) ligands, and four BF₄⁻ necessary in case of four neutral ligands being present). This observation corresponds to a mixture of 0.25 carboxylate and 0.75 carboxylic acid; therefore, the correct mean composition in the solid-state should be [Pd₂L₂L₂*]³⁻ with **L2*** depicting the deprotonated carboxylate form of **L2** (Figure 2A). Also, the C-O distances show similar values of 1.308(11) and 1.315(14) Å, which normally indicates the presence of (deprotonated) carboxylates. However, intermolecular hydrogen bonding similarly should have an influence on the bond distances and might lead to adaptation of the C=O and C–OH bonds. Therefore, combined with the charge balance argument, we conclude that both carboxylate and carboxylic acid groups are present and the latter contribute to the packing.

Since cages based on phenyl-centred *endo*-functionalised ligands like **L1** or **L2** are assumed to possess a more hydrophobic pore than their pyridyl-centred analogues (discussion *vide supra*), we also investigated the electrostatic potential (ESP) of the cage and its cavity (for the fully deprotonated state). To this aim, we performed a single point calculation using Gaussian 16.B.01 with hybrid functional B3LYP, basis set def2-SVP and the molecular cage geometry as experimentally obtained by single crystal- (SC-)XRD. In Figure 2B, the ESP is

mapped onto the van der Waals surface of the $[\text{Pd}_2\text{L}_2^*]_4$ cage and the surface extrema including their values (in kcal/mol) are shown. Hereby, red areas indicate negative values, blue areas positive values, and white neutral areas, showing that the inside of the cavity is mainly neutral at the equatorial positions of the linker, and slightly more electron-deficient towards the vertices containing the Pd^{2+} ions. Areas showing a significant negative ESP of $[\text{Pd}_2\text{L}_2^*]_4$ are only observed for the carboxylate groups of the *exo*-functionalisation, while the cage itself shows significantly more positive areas (Fig. 2B). The global maximum (68.24 kcal/mol) is located at the hydrogen atom of the pyridine unit, whereas another maximum is located at the hydrogen of the phenyl unit (16.50 kcal/mol). The global minimum (-91.06 kcal/mol) is found close to the alkyne moiety going along with the high π -electron density at these carbon atoms, while another surface minimum corresponds equally to the hydrogen atoms of the pyridine units inside the cavity. This result is in line with the above-mentioned hypothesis of a comparably hydrophobic cavity of our cages.

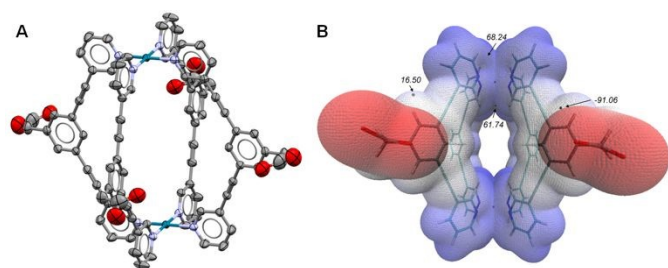


Figure 2 – A) Molecular structure of Pd_2L_4 -cage scaffold with partially deprotonated ligand L_2 ($[\text{Pd}_2\text{L}_2^*]_4^{2-}$ with L_2^* being deprotonated L_2) in the solid state. Atoms are displayed as ellipsoids with ADPs given at 50% probability. Hydrogen atoms are omitted for clarity, carbon is displayed in grey, nitrogen in light purple, Pd in turquoise and oxygen in red. B) ESP-mapped molecular VdW surface of $[\text{Pd}_2\text{L}_2^*]_4$ given in kcal/mol. Surface maxima (grey) and minima (black) are displayed and labelled with the corresponding potential (in kcal/mol).

Photophysical properties and stability in aqueous environment

The emission properties and quantum yield of fluorescence (QY, ϕ_F) of the new cages (**CG1.X** and **CG2.BF₄**), corresponding ligands (**LG1** and **LG2**) and BODIPY fluorophore (**G1**) were investigated using fluorescence spectroscopy. The results are presented in Table 1 (Figure S18) and show an excitation wavelength in the visible region (ca. 525 nm). Notably, the quantum yield of the amine-functionalised BODIPY fluorophore **G1** is quite low (6%) compared to previously reported ligand-BODIPY fluorophore ($\phi_F = 72\%$),^{17,19} attributable to the quenching effect of the amine substituted aromatic ring. However, coupled to the carboxylic acid of the bipyridyl ligand, the resulting **LG1** conjugate displayed an excellent quantum yield value of 82%. Intriguingly, the introduction of another carbon centre between the aromatic pyridyl ligand and the fluorophore in **LG2** resulted in ca. 20% loss of the QY. Overall, these data suggest the involvement of the aromatic system of the pyridyl scaffold in the ligand's emissive properties. Of note,

cage **CG1.X** even outperformed the quantum yields of previously investigated BODIPY-cages (ϕ_F ca. 60%)²⁴.

Table 1. Photophysical data acquired by UV-Visible spectrophotometry and fluorescence spectroscopy in DMSO for the BODIPY fluorophore (**G1**), BODIPY functionalised bipyridyl ligand (**LG1**), and the BODIPY- $[\text{Pd}_2\text{L}_4]^{4+}$ metallacages (**CG1.X** and **CG2.BF₄**).

Compound	λ_{max} (Abs) [nm]	ϵ_{max} [$\text{M}^{-1}\text{cm}^{-1}$]	λ_{max} (Em) [nm]	ϕ_F [%] ^a
G1	525	61 500	539	6
LG1	290, 525	80 000	541	82
LG2	287, 525	111 643	541	62
CG1.BF₄ / CG1.NO₃	290, 525	228 600	541	80
CG2.BF₄	287, 525	332 319	541	67

^a Reference standard for QY assessment was Rhodamine 6G ($\phi = 94\%$ in degassed EtOH at room temperature).

The stability of the metallacages in both water and phosphate buffered saline (PBS, pH 7.4) was then studied by UV-Visible spectrophotometry. As shown in Figure 3, the absorption spectra of both **CG1.NO₃** and **CG2.BF₄**, featuring two main bands at ca. 300 and 530 nm, were stable in water over 24 h. The same behaviour was recorded for **CG1.BF₄** (data not shown). Interestingly, the **CG1.NO₃** metallacage was also sufficiently stable in PBS solution (pH 7.4) with a loss of 7% over the first hour of buffer exposure, although marked reduction (ca. 50%) of the two absorption bands was observed after 6 h incubation and continued over the 24 h period. Over time, formation of a precipitate was detected in solution, and shaking of the cuvette partly restored the original absorption spectrum, suggesting that the overall cage scaffold remained unaltered. This behaviour is in line with previously reported studies on *exo*-functionalised BODIPY- $[\text{Pd}_2\text{L}_4]^{4+}$ cages,²⁴ although with an improvement of the stability in buffered solution.

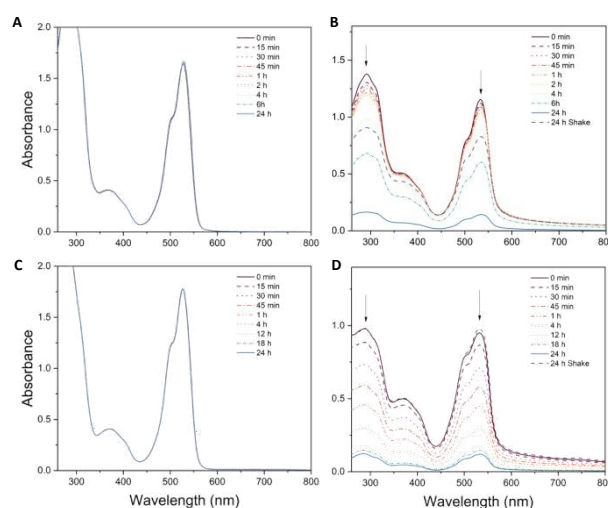


Figure 3 – UV-visible spectra of **CG1.NO₃** and **CG2.BF₄** in water (A, C) and in 1x PBS (B, D) recorded over 24 h.

On the contrary, the stability studies of the **CG2.BF₄** cage in PBS solution (Figure 3C and 3D) evidenced an important reduction of its characteristic band already after 1 h (ca. 40%), which became more prominent (up to 87%) over 24 h. As the maximum absorbance could be restored upon cuvette shaking, it could be concluded that the observed phenomenon was due to the precipitation of the cage. It is worth noting that the solubility of metallacages is determined by a number of factors, including the hydrophilic/hydrophobic character of the ligand scaffold, the type of metal ion, as well as the counter ion balancing the cage's overall positive charge. The latter can also be subjected to exchange with buffer components. Due to this complex interplay, it is difficult to discriminate what causes cage precipitation and/or instability in solution.

Stability towards glutathione (GSH)

[Pd₂L₄]⁴⁺ metallacages have been reported to undergo disassembly in the presence of the intracellular reducing agent glutathione (GSH).^{24,30} Physiologically, human plasma GSH concentrations average 0.3 – 0.5 mM, while intracellular values are in the range 1-2 mM, although there is a heterogeneity of concentration depending on cell type and organelle.³¹ Therefore, the reactivity of the BODIPY-functionalised cages **CG1.BF₄** and **CG2.BF₄** exposed to 2 mM GSH was monitored by ¹H NMR spectroscopy in DMSO-*d*₆:D₂O (9:1) over 18 h. Upon addition of GSH, the **CG1.BF₄** cage can dissociate into the precursor **LG1**, as shown by the appearance of the characteristic ligand's signals of protons H_a' and H_b' (at 8.75 and 8.56 ppm, respectively) immediately after mixing (Figure S19). However, while it is clear that cage disassembly started immediately after GSH addition, the cage signals remain evident in solution even after 18 h incubation; only ca. 8% dissociation was calculated (by comparing the integral value of peak H_b of the metallacage to the corresponding signal H_b' of the ligand) within the first 30 min. It must be noted that quantitative monitoring of the process over time (> 30 min) was prevented by the poor solubility of **LG1** in the selected experimental conditions; nevertheless, only addition of an excess GSH (4 mM) leads to the marked appearance of the free ligand signal.

Cage **CG2.BF₄** shows a similar behaviour with ca. 15% disassembly observed after 10 min (Figure 4). **LG2** is, however, more soluble in the selected experimental conditions than **LG1**, its ¹H NMR signals could be monitored along the entire experiment runs. Overall, 80% of **CG2.BF₄** remained in solution even after 18 h, and the disassembly process could progress further only in the presence of an excess of GSH (4 mM). The obtained results suggest that the metallacages are likely to show limited intracellular disassembly in response to GSH.

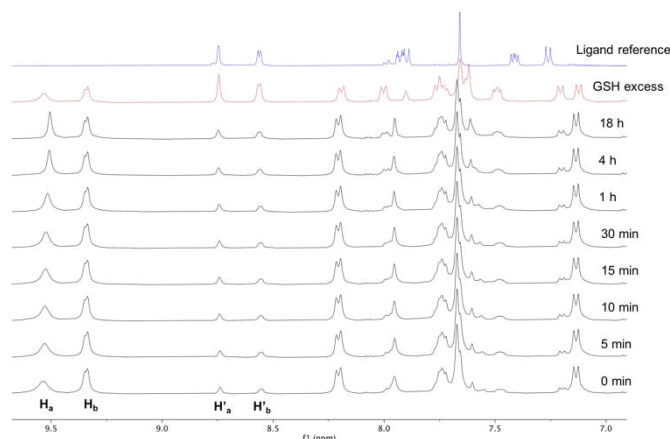


Figure 4 - Stacked ¹H NMR spectra of ligand **LG2** (blue spectrum, DMSO-*d*₆) and the corresponding metallacage **CG2.BF₄** (second trace from top) after addition of 1 equiv. glutathione (GSH, 2 mM) in 9:1 ratio of DMSO-*d*₆: D₂O, followed over time. A further addition of excess GSH (4 mM) was performed after 18 h to further monitor cage dissociation (red spectrum).

Cisplatin encapsulation studies

¹H NMR spectroscopy

To demonstrate encapsulation of cisplatin within the Pd₂L₄ metallacages, ¹H NMR spectroscopy with DMF-*d*₇ as solvent was applied. Spectra were recorded prior and after addition of two equiv. of cisplatin vs one equiv. of **CG1.BF₄** or **CG2.BF₄** and compared. A representative zoomed overlay spectrum displaying **CG1.BF₄** and [(cisplatin)₂⊂**CG1.BF₄**] is shown in Figure 5, whilst similar spectrum of **CG2.BF₄** and [(cisplatin)₂⊂**CG2.BF₄**] host-guest complex is reported in the supplementary information (Figure S20A). In both cases, the two signals corresponding to the protons facing the internal cavity (H_a and H_e), as well as the signal of the *exo*-facing proton (H_b), were observed to undergo chemical shifts due to cisplatin encapsulation, as previously reported.²⁴ Specifically, a downfield shift was observed for H_a and H_e of +0.02 ppm and +0.06 ppm, respectively, accompanied by a broadening of the signals. Similarly, H_b featured a downfield shift of +0.02 ppm.

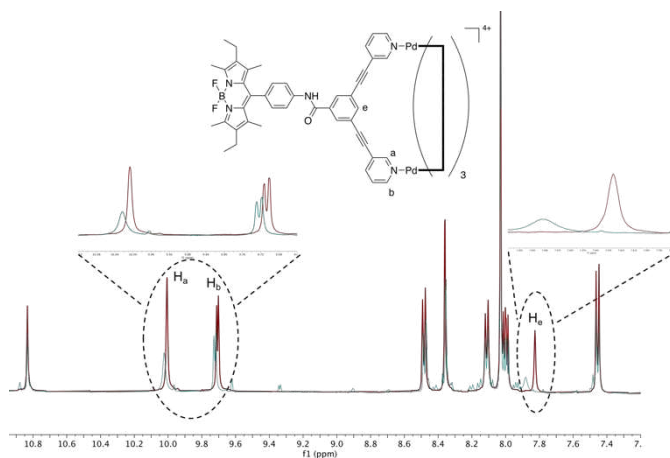


Figure 5 – Cisplatin encapsulation in a metallacage. Stacked ¹H NMR spectra of cage **CG1.BF₄** in DMF-*d*₇ (red trace) alone and after the addition of 2 equiv. of cisplatin (green trace) to form the [(cisplatin)₂⊂**CG1.BF₄**] host-guest complex. The region of the spectrum between 5-3.5 ppm is included in Figure S20B in comparison to free cisplatin.

Uptake and cellular localisation studies in melanoma A375 cells

Cell uptake of cages and ligands in A375 fixated cells

Initially, cancer cell uptake was investigated by incubating A375 cells with non-toxic concentrations (5 μ M) of fluorophore **G1**, ligand **LG1**, and cage **CG1**, respectively, for 2 h at different temperatures, and imaged by fluorescence microscopy. By lowering the temperature to 4 °C, active endocytic mechanisms facilitating transport across the plasma membrane are inhibited. It should be noted that, as expected, cage **CG1.BF₄** behaved as **CG1.NO₃** in all the cell experiments reported in this manuscript, and therefore, in several cases, we show here only representative results for one of the two cage complexes. Due to its lower solubility in physiologically compatible media and lower QY, the **CG2.BF₄** cage was not considered for further in-depth biological application. Interestingly, the fluorophore **G1** maintains marked cellular fluorescence at 4 °C indicating an energy independent transport mechanism for cell entry (Figure 6). In fact, **G1** is most likely present as a neutral species in the medium and likely to diffuse across the plasma membrane. Instead, a distinct reduction in the fluorescence signal at 4 °C is observed for the ligand **LG1** and cage **CG1**, implying that cellular uptake only occurs by active transport.

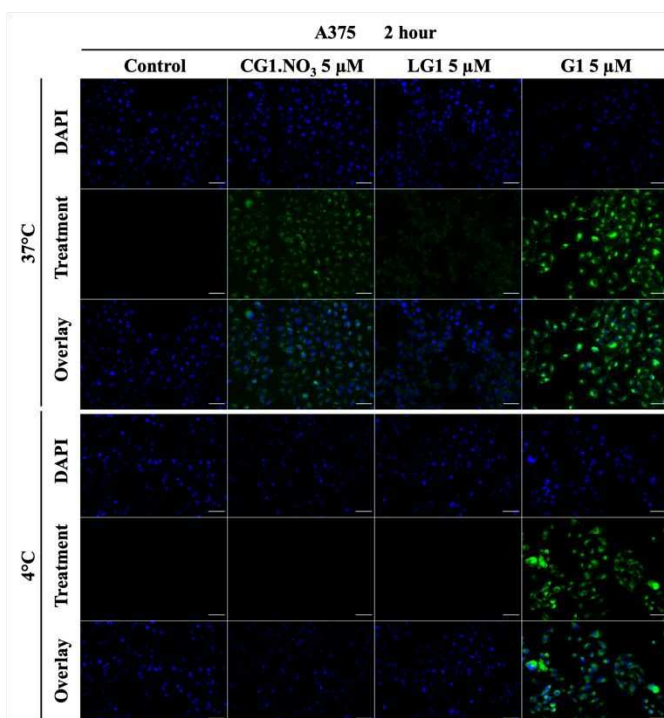


Figure 6 – Fluorescence widefield microscopy images of fixed human A375 cells incubated with (5 μ M) or without **CG1.NO₃**, **LG1** or **G1** for 2 h at 37 °C or 4 °C. Counterstaining of nucleus with DAPI. Scale bar 50 μ m.

Further CLSM investigation confirmed a distinct pattern of sub-cellular localisation for each compound in fixed A375 cells (Figure 7). **CG1** showed only a moderate fluorescence intensity in the cytosol, mostly accumulating in cell periphery, and notably, spherical vesicles. The localisation of **G1** and **LG1** was also noticeable in these structures of quite uniform dimensions, in line with our previous studies on similar cage systems.²⁴

Furthermore, there was no significant evidence of nuclear entry.

Live cells confocal microscopy studies

To exclude possible interferences of the cell fixation protocol on the fluorescence patterns, we repeated the experiments using live cells with the plasma membrane labelled with CellMask Deep Red™ (Figure 8). The results confirm the presence of both **LG1** or **CG1** in intracellular vesicles, residing within the defined plasma membrane borders (Figure 8). Accumulation is more pronounced near the cell periphery, and the vesicles again appear to be quite homogenous in size, and sometimes observed as grape-like clusters. Optical dissection of the cells using z-oriented slices confirms the intracellular localisation of cage **CG1** (see Figure 8B and z-stack of complete image in SI, Figures S21 and S22). Again, there was no evidence of cage and ligand accumulation in the nucleus.

A time-lapse movie and subsequent quantification of **CG1** (5 μ M) cell uptake (Movie 1 and Figure S23 in the supplementary material) was performed on live A375 cells, imaged under tissue culture conditions. After ca. 4 min of equilibration, XYT-images were obtained with a 30 sec time interval for 1 h.

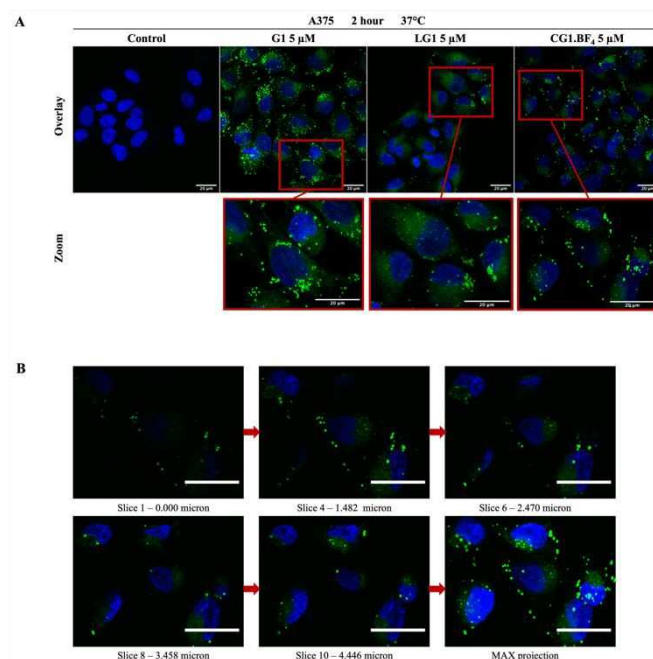


Figure 7 - A) CLSM images and zoomed areas of fixed human A375 cells pre-treated with 5 μ M **G1**, ligand **LG1** or cages **CG1.BF₄** for 2 h at 37 °C; B) Different z-slices of the cells from bottom to top are shown, as well as the maximum projection of the stack. Counterstaining of nuclei with DAPI. Scale bar 20 μ m.

Cells treated with **CG1** did not lead to pronounced morphology alterations indicating limited short-term toxicity of the cage (brightfield in Figure S23A). Moreover, cell uptake and accumulation in vesicles become evident from 30 min incubation and quantifying the fluorescent intensity shows a gradual increase in intensity over time, seemingly approaching a plateau at the end of the acquisition (Figure S23B). This could be caused by several factors, such as saturated receptor

mediated uptake, limiting intracellular accumulation, or due to the luminescence properties of the cage, as prolonged excitation might degrade the chromophore or influence its structural integrity. This experiment also served to highlight the excellent photostability of the developed BODIPY-cage complex.

Early endosome immunolabeling

The intracellular accumulation of **CG1** observed in vesicles in combination with an active mode of transport for both ligand and cage suggest an endosomal form of uptake. Immunolabeling of the peripheral early endosomal marker EEA1²⁴ was used to evaluate whether cages and ligands were exploiting transport through the early endosome in human A375 cells. Cells were pre-incubated up to 2 h with either 5 μ M **LG1** or **CG1** before immunolabelling (Figure 9) and **LG1** showed minimal colocalisation with EEA1 despite trafficking to the same juxtanuclear location. In addition, the cage **CG1**, showed no colocalisation between the bright vesicular structures seen previously and EEA1, indicating that the cages are highly unlikely to be entering via EEA1 labelled structures, known to be implicated in endosomal transport of other markers such as transferrin.³²

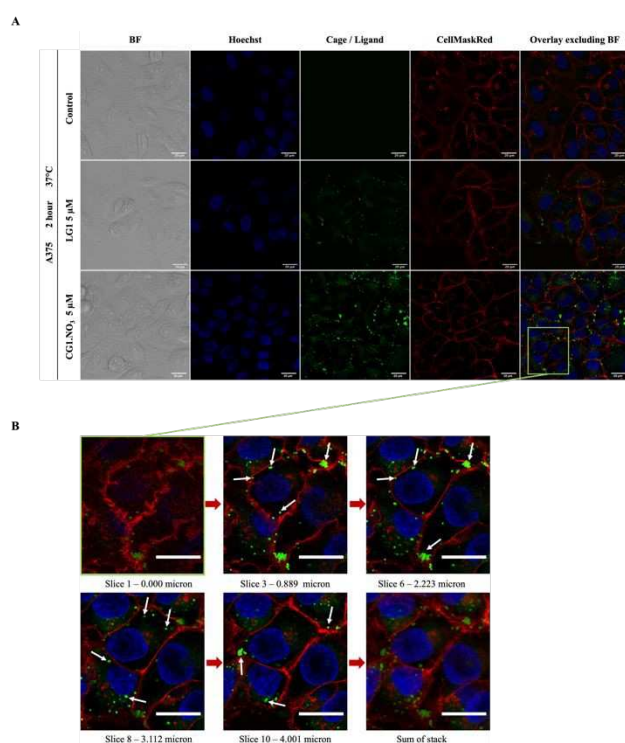


Figure 8 – CLSM images of live A375 cells incubated with A) 5 μ M of **LG1** or **CG1.NO₃** for 2 h; B) a zoomed selection of images along the z-axis from A) as highlighted in the overlay slice of **CG1.NO₃** (square). Arrowheads highlight intracellular vesicles and vesicle clusters. BF = bright field. Images enhanced after acquisition. Counterstaining of nucleus with DAPI. The plasma membrane was counterstained with CellMask™ Deep Red and of nuclei with Hoechst 33342. Scale bar 20 μ m.

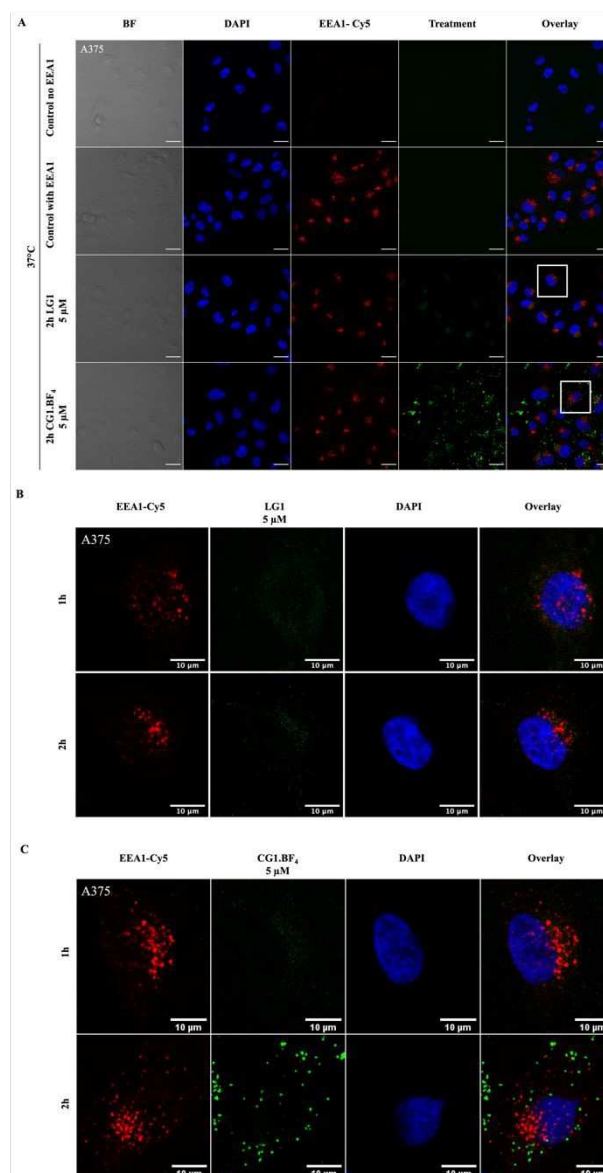


Figure 9 - A) CLSM images of fixed A375 cells exposed to 5 μ M of **LG1** or **CG1.BF₄**. Early endosomes labelled with EEA1-Cy5. Counterstaining of nucleus with DAPI. Scale bar is 20 μ m. Zoomed image of single cells incubated for 1 h and 2 h with 5 μ M of B) **LG1** and C) **CG1.BF₄**. Scale bar 10 μ m.

Lysosome accumulation studies

To investigate whether the compounds traffic to lysosomes **LG1**, **CG1.NO₃** and **CG1.BF₄**, a colocalisation experiment was conducted whereby the lysosomes were pre-loaded with the fluid phase endocytosis probe Dex-647.³³ Live cell images were acquired after 3 h incubation with ligand, cage or Dex-488 alone as a control probe. Both the cage and ligand showed little colocalisation with lysosomal Dex-647 after incubation at this time point when compared to Dex-488 which showed moderate colocalisation (Figure 10). To confirm the separation of cage and lysosomal signals a line profile was plotted showing **CG1.BF₄** and the lysosomal marker are localized to different compartments (Figure 11). This is in contrast to Dex-488 uptake

showing strong colocalisation. These results were confirmed using Pearsons and Manders correlation coefficients showing that all cages and ligands have poor colocalisation with lysosomal structures, with dextran accumulating in these organelles in a time dependent manner (Figure S24)^{34,35}.

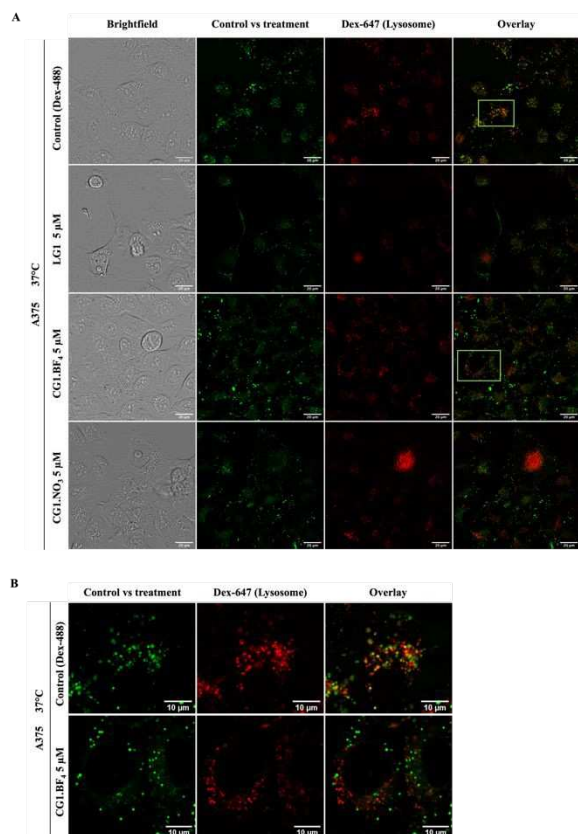


Figure 10 - A) CLSM images of human A375 cells with lysosomes labelled using pulse-chased with Dex-647 (red) and incubated with 5 µM of **CG1.BF₄** cage, **CG1.NO₃** cage, ligand **LG1** or 200 µg/mL Dex-488 (green) and imaged after 3 h. Scale bar is 20 µm. **B)** Zoom of sections indicated in **A)**, highlighting a certain colocalisation of control Dex-488 with lysosomal dye Dex-647 (yellow), but a clear separation compared to the cage's fluorescence. Scale bar 10 µm.

Enlarging the fluorescence images of the cage-treated cells overlaid with the corresponding bright field image, it was possible to identify colocalisation of the fluorescence with some dark intracellular vesicles. We hypothesised that these correspond to melanosomes, present in this cell line (Figure 12).³⁶ Melanosomes are unique melanocyte-specific intracellular organelles and are involved in the synthesis and storage of melanin pigments.³⁷

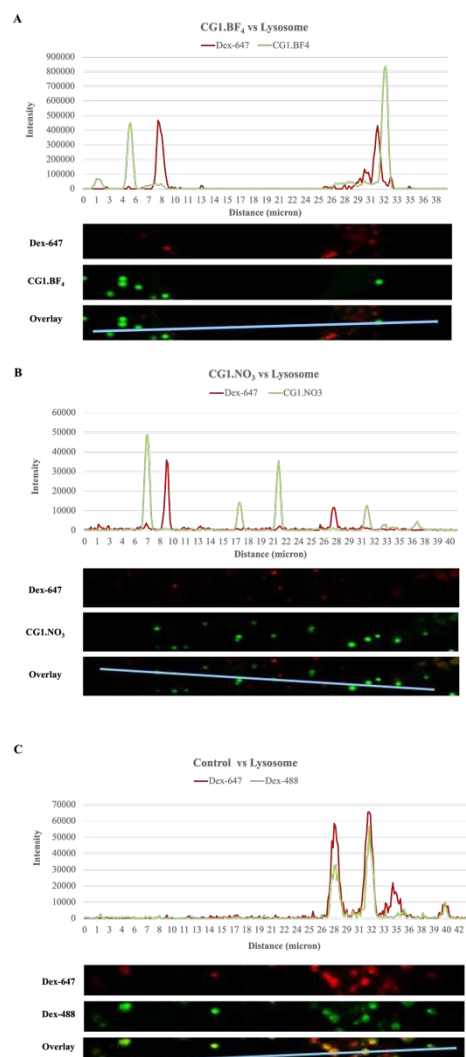


Figure 11 - Graph displaying the intensities of pixels along a line (illustrated in overlay) within the image of A375 cells treated with the lysosomal marker Dex-647 (red) and **A)** **CG1.BF₄** (green) **B)** **CG1.NO₃** (green) and **C)** Dex-488 cells (green) at 3 h incubation. The x-axis represents distance along the blue line and the y-axis is the pixel intensity.

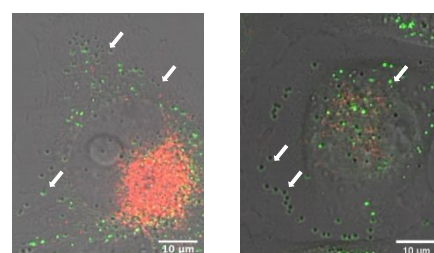


Figure 12 - CLSM image of single A375 cells incubated for 2 h with **CG1.NO₃** (left) and **CG1.BF₄** (right) after pulse with lysosomal dye Dex-647. Arrows highlight intracellular compound accumulation overlap with dark pigmented vesicles. Overlay of brightfield, **CG1.BF₄** / **CG1.NO₃** (green) and Dex-647 (red). Scale bar 10 µm.

Antiproliferative activities and intracellular accumulation in different cancer cell lines

The possibility that the cages could accumulate in melanosomes in A375 cells prompted us to study the sub-cellular

accumulation of the metallacages in non-melanoma cell lines. In addition, we wanted to evaluate the effects of cisplatin encapsulation on the intracellular distribution of the metallacages. However, before further microscopy studies, ligand **LG1**, cage **CG1.BF₄** as well as the $[(\text{cisplatin})_2\text{CG1.BF}_4]$ complex were tested for their antiproliferative effects in different cancer cell lines in comparison to free cisplatin. Thus, human breast cancer SK-BR-3 and MCF7 cells, as well as melanoma A375 cells were selected. The EC₅₀ values after 24 h incubation are reported in Table 3, and show that the ligand **LG1** and the **CG1** cage are non-toxic towards the three cell lines up to the maximum concentration tested. Moreover, only in the case of SK-BR-3 cells was there a notable increase of the antiproliferative activity of the $[(\text{cisplatin})_2\text{CG1.BF}_4]$ complex compared with free cisplatin; while no difference was recorded in A375 and MCF7 cells. The same results were obtained for cage **CG1.NO₃** (data not shown) which further confirmed the non-influence of the counter ion.

Table 3 - Antiproliferative activity (EC₅₀ values) of ligand **LG1**, cages **CG1.BF₄** as well as of the $[(\text{cisplatin})_2\text{CG1.BF}_4]$ complex against human A375, SK-BR-3 and MCF7 cells after 24 h incubation, compared to cisplatin. Measured using CellTiter Blue assay.

Compound	EC ₅₀ (μM) ^a		
	A375	SK-BR-3	MCF-7
LG1	>50	>50	>30
CG1.BF₄	>50	>50	>30
$[(\text{cisplatin})_2\text{CG1.BF}_4]$ ^b	30.0 ± 1.9	29 ± 5	>30
cisplatin	33.9 ± 2.9 ^c	>50	>30

^a Data is presented as mean ± SEM of at least three independent experiments unless otherwise indicated.

^b The EC₅₀ is calculated with respect to the concentration of free cisplatin. ^c Value from ref.³⁸

Subsequently, CLSM of live SK-BR-3 and MCF7 treated with $[(\text{cisplatin})_2\text{CG1.BF}_4]$ was acquired in comparison to A375 cells (Figure 13). In the latter cell line, the presence of encapsulated cisplatin did not influence cage uptake and sub-cellular distribution compared to the studies performed using the “empty” **CG1** described above. Thus, cage accumulation is observed in putative melanosomes and no fluorescent signal is detected in the nuclei. Conversely, the intracellular distribution profile is quite different in the case of SK-BR-3 cells, whereby, the fluorescence signal of the $[(\text{cisplatin})_2\text{CG1.BF}_4]$ complex is observed throughout the cytoplasm including a few well-defined vesicular structures that are shown in the z-stack images (Figure 14). Such different sub-cellular localisation may account for the observed enhanced cytotoxic effect of $[(\text{cisplatin})_2\text{CG1.BF}_4]$ in SK-BR-3 cells (Table 3). In MCF7 cells, no trace of **CG1** uptake was observed (Figure S25), which is in line with the lack of enhanced antiproliferative effects vs free cisplatin shown above (Table 3).

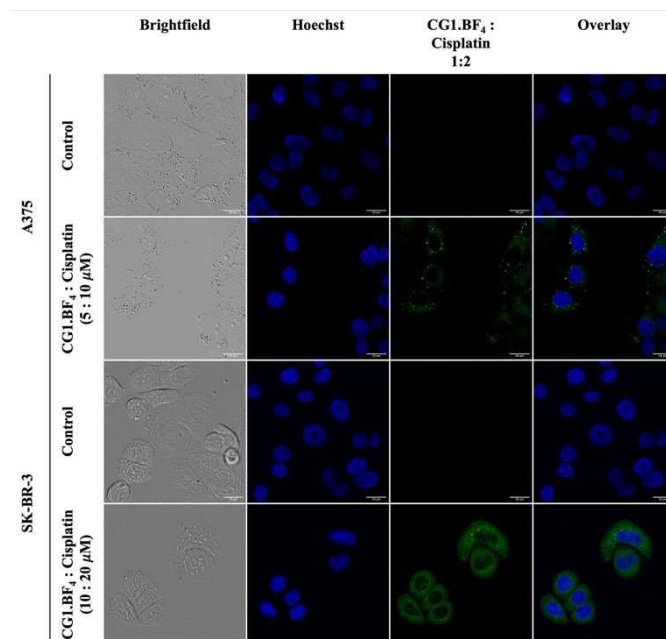


Figure 13 - CLSM images of live A375 and SK-BR-3 cells incubated with different concentrations of $[(\text{cisplatin})_2\text{CG1.BF}_4]$ for 2 h at 37°C with 5% CO₂. Counterstaining of nucleus with Hoechst. Images enhanced after acquisition. Scale bar 20 μm.

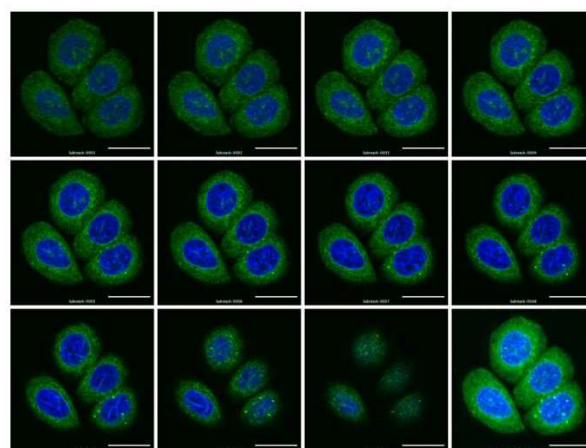


Figure 14 - Z-stack CLSM images of live SK-BR-3 cells incubated with $[(\text{cisplatin})_2\text{CG1.BF}_4]$ [20:10 μM] for 2 h. Counterstaining of nucleus with Hoechst. Top left image starts at the cell base, z-stack moving upwards. Last slice is the maximum projection of the stack. Images enhanced after acquisition. Scale bar 20 μm.

Experimental

General

Chemicals. All reagents and solvents were obtained from commercial suppliers and used without further purification, unless otherwise stated. Triethylamine was distilled under nitrogen before use. Cisplatin was purchased at Sigma-Aldrich (CAS number 15663-27-1). ¹H NMR, ¹³C{¹H} NMR and ¹¹B NMR spectra were recorded on a 500 MHz DMX (Bruker) or 400 MHz AV spectrometer (Bruker). Chemical shifts are given in parts per million (ppm). Abbreviations for NMR multiplicities are: singlet (s), doublet (d), triplet (t), quartet (q), doublet of doublets (dd), doublet of triplets (dt) and multiplet (m). Coupling constants *J*

are given in Hz. The following solvents were used as internal standards: DMSO- d_6 : 2.50 ppm (^1H NMR) and 39.52 ppm (^{13}C NMR); CDCl_3 : 7.26 ppm (^1H NMR) and 77.16 ppm (^{13}C NMR); acetone- d_6 : 2.05 ppm (^1H NMR) and 29.84 ppm (^{13}C NMR); DMF- d_7 : 8.03 ppm (^1H NMR) and 163.15 ppm (^{13}C NMR). High resolution ESI-HR-MS spectra were recorded either on a Walter Synapt G2SI QTOF or on a Thermo Fisher Exactive Plus Orbitrap mass spectrometer.

Synthesis of ligands

3,5-Dibromobenzoate, Benzyl 2-(3,5-Dibromophenyl)acetate, 3,5-Bis(pyridin-3-ylethynyl)benzoate, Benzyl-2-(3,5-bis(pyridine-3-ylethynyl)phenyl)acetate, 3,5-Bis(pyridin-3-ylethynyl)benzoic Acid (**L1**), 2-(3,5-bis(pyridine-3-ylethynyl)phenyl)acetic acid (**L2**) and the BODIPY-NH₂ fluorophore (**G1**, Scheme S1), have been synthesised adapting previously reported procedures, and the analytical data are in accordance with the literature.²¹

LG1 and LG2. A mixture of **G1** (1.00 eq.), **L1** or **L2** (1.00 eq.), CMPI (4.00 eq.) and DMAP (10.0 eq.) was dissolved in anhydrous DMF (10 mL) and stirred under a nitrogen atmosphere at 130 °C. After 22 h, the solvent was removed under reduced pressure, the residue dissolved in DCM (60 mL) and washed with water (3x 40 mL) and brine (1x 40 mL). The organic layer was dried over MgSO_4 and filtered over a glass-fritted funnel (pore 3). The solvent was removed under reduced pressure and the crude compound purified *via* silica column chromatography (EtOAc : n -hexane = 3:1 \rightarrow 5:1) re-dissolved in a small amount of DCM, crushed out with an excess of n -hexane and filtered through filter paper.

LG1: G1 (85.4 mg, 216 μmol), **L1** (73.0 mg, 225 μmol), CMPI (223 mg, 948 μmol), DMAP (280 mg, 2.29 mmol). Red solid, yield: 48.9 mg, 69.7 μmol , 32%.

^1H NMR (400 MHz, acetone- d_6): δ [ppm] = 10.02 (s, 1H, NH), 8.82 (d, J = 1.3 Hz, 2H, H_a), 8.63 (dd, J = 1.7, 4.9 Hz, 2H, H_b), 8.25 (d, J = 1.6 Hz, 2H, H_f), 8.13 (d, J = 8.5 Hz, 2H, H_g), 8.07 – 7.95 (m, 3H, H_d , H_e), 7.48 (dd, J = 4.9, 7.9 Hz, 2H, H_c), 7.40 (d, J = 8.5 Hz, 2H, H_h), 2.50 (s, 6H, NCCH_3), 2.37 (q, J = 7.5 Hz, 4H, CH_2CH_3), 1.44 (s, 6H, CCH_3), 1.00 (t, J = 7.5 Hz, 6H, CH_2CH_3).

^{13}C NMR (126 MHz, acetone- d_6): δ [ppm] = 180.6, 165.9, 164.5, 154.3, 153.0, 150.3, 145.1, 141.5, 140.9, 139.4, 137.7, 137.3, 131.9, 131.6, 129.8, 124.5, 124.4, 121.5, 120.4, 91.1, 88.5, 17.5, 15.0, 12.6, 12.2.

^{11}B NMR (160 MHz, acetone- d_6): δ [ppm] = 0.70.

HRMS (ESI, MeOH): calcd. for $\text{C}_{44}\text{H}_{38}\text{BFN}_5\text{O}$ [M-F]²⁺: m/z = 341.6620; found: 341.6582.

LG2: G1 (100 mg, 253 μmol), **L1** (85.6 mg, 253 μmol), CMPI (259 mg, 1.01 mmol), DMAP (309 mg, 2.53 mmol). Red solid, yield: 45.0 mg, 62.9 μmol , 25%.

^1H NMR (400 MHz, acetone- d_6): δ (ppm) = 9.78 (s, 1H, NH), 8.78 (d, J = 1.5 Hz, 2H, H_a), 8.59 (dd, J = 4.8, 1.5 Hz, 2H, H_b), 7.96 (dt, J = 7.9, 1.5 Hz, 2H, H_f), 7.93 (d, J = 8.7 Hz, 2H, H_i), 7.69 (s, 3H, H_e , H_f), 7.44 (ddd, J = 7.9, 4.8, 1.5 Hz, 2H, H_c), 7.29 (d, J = 8.7 Hz,

2H, H_h), 3.88 (s, 2H, H_g), 2.48 (s, 6H, NCCH_3), 2.33 (q, J = 7.6 Hz, 4H, CH_2CH_3), 1.37 (s, 4H, CCH_3), 0.97 (t, J = 7.6 Hz, 6H, CH_2CH_3). **^{13}C NMR** (101 MHz, acetone- d_6): δ (ppm) = 169.5, 154.4, 153.0, 150.2, 141.4, 141.2, 139.4, 139.3, 138.3, 134.0, 133.7, 133.6, 131.8, 131.4, 129.9, 124.4, 124.2, 120.8, 120.7, 92.0, 87.8, 44.0, 17.6, 15.1, 12.7, 12.3.

^{11}B NMR (128 MHz, acetone- d_6): δ (ppm) = 0.78.

HRMS (ESI, DCM:DMF 1:1) for $\text{C}_{45}\text{H}_{40}\text{BFN}_5\text{O}$ [M-F]⁺: m/z = 696.3304; found: 696.3301.

Synthesis of metallacages

A solution of Pd^{2+} precursor (2.00 eq.) and ligand (4.00 eq.) in DMSO was stirred at r.t. for 1 (**CG1.X**) or 2 h (**CG2.BF₄**) (Scheme S1). Afterwards, precipitation by addition of acetone and diethyl ether and consecutive filtration gave the respective cages **CG1.NO₃**, **CG1.BF₄** and **CG2.BF₄**.

CG1.X. Ligand **LG1** ($\text{X} = \text{NO}_3$, 32.1 mg, 45.8 μmol , 4.00 eq.; $\text{X} = \text{BF}_4$, 55 mg, 78 μmol , 4.00 eq) was dissolved in DMSO (3 mL) prior to the addition of 2 eq. of the Pd precursor ($\text{X} = \text{NO}_3$, $\text{Pd}(\text{NO}_3)_2 \cdot 2 \text{H}_2\text{O}$, 6.30 mg, 23.6 μmol ; $\text{X} = \text{BF}_4$, $\text{Pd}(\text{NCCH}_3)_4 \cdot 2 \text{BF}_4$, 17 mg, 39 μmol) After 1 hour under vigorous stirring at r.t., acetone (4.5 mL) was added, along with excess of diethyl ether to precipitate the product. The mixture was further stirred for 10 min, before filtering it over a glass-fritted funnel (pore 4) to yield the metallacage as a red solid ($\text{X} = \text{NO}_3$, 29.3 mg, 8.97 μmol , 78%; $\text{X} = \text{BF}_4$, 57 mg, 18 μmol , 86%).

^1H NMR (500 MHz, DMSO- d_6): δ [ppm] = 10.74 (s, 1H, NH), 9.80 (s, 2H, H_a), 9.44 (d, J = 5.7 Hz, 2H, H_b), 8.31 (s, 4H, H_d , H_f), 8.13 (s, 1H, H_e), 7.95 (d, J = 8.1 Hz, 2H, H_g), 7.87 (t, J = 7.1 Hz, 2H, H_c), 7.34 (d, J = 8.3 Hz, 2H, H_h), 2.43 (s, 6H, NCCH_3), 2.28 (s, 4H, CH_2CH_3), 1.31 (s, 6H, CCH_3), 0.93 (s, 6H, CH_2CH_3).

^{11}B NMR (128 MHz, DMSO- d_6): δ [ppm] = 0.76.

HRMS (ESI, MeOH): calcd. for $\text{C}_{178}\text{H}_{157}\text{B}_4\text{F}_7\text{N}_{20}\text{O}_6\text{Pd}_2\text{Na}_2$ [$\text{M-4NO}_3\text{-F-2H+2MeOH+2Na}$]²⁺: m/z = 1554.5469; found: 1554.0194.

CG2.BF₄. **LG2** (30.0 mg, 41.9 μmol , 4.00 eq.) was dissolved in DMSO (1.5 mL) prior to the addition of $\text{Pd}(\text{CH}_3\text{CN})_4(\text{BF}_4)_2$ (9.31 mg, 21.0 mmol, 2.00 eq.). After 2 hours at r.t., acetone (3 drops) was added, the desired product crushed out with an excess of EtO_2 and filtered through a glass filter funnel pore 5 (32.1 mg, 9.38 μmol , 90%, red solid).

^1H NMR (400 MHz, DMSO- d_6): δ (ppm) = 10.43 (s, 1H, NH), 9.62 (s, 2H, H_a), 9.39 (d, J = 5.6 Hz, 2H, H_b), 8.28 (d, J = 8.1 Hz, 2H, H_d), 7.90 (s, 1H, H_e), 7.83 (m, 2H, H_c), 7.73 (m, 4H, H_f , H_i), 7.24 (d, J = 8.6 Hz, 2H, H_h), 3.80 (s, 2H, H_g), 2.40 (s, 6H, H_o), 2.25 (q, J = 7.8 Hz, 4H, H_m), 1.25 (s, 4H, H_l), 0.90 (t, J = 7.8 Hz, 6H, H_n). **^{11}B NMR** (128 MHz, $\text{CD}_3\text{CN-}d_6$): δ (ppm) = 0.82, -0.71.

HRMS (ESI, DCM : DMF 1:1): calcd. for $\text{C}_{180}\text{H}_{160}\text{B}_4\text{F}_8\text{N}_{20}\text{O}_4\text{Pd}_2$ [M]⁴⁺: m/z = 768.5327; found: 768.5325.

X-ray diffraction studies

Crystals of cage $[\text{Pd}_2\text{L}_2\text{L}_2^*]_3(\text{BF}_4)_3$ were obtained by vapor diffusion method. For this purpose, 4 eq. **L2** (2.50 mg) and 2 eq. $\text{Pd}(\text{CH}_3\text{CN})_4(\text{BF}_4)_2$ precursor (1.64 mg) were dissolved in 1 mL

DMF and added to a glass tube. The solution was stirred for 60 min to enable cage formation. Afterward, 60 μ L acetone were added to this solution to facilitate the miscibility with the second solvent. The tube was then transferred into a second larger container containing 5 mL diethyl ether. The whole set-up was sealed with parafilm. Crystal formation took up to 4 days at room temperature. X-ray intensity data were collected on a Bruker D8 Venture single crystal X-Ray diffractometer equipped with a CMOS detector (Bruker Photon-100), a TXS rotating anode with MoK α ($\lambda=0.71073$ Å) and a Helios mirror optic using the software package APEX3.³⁹ Measurements were performed on single crystal coated with perfluorinated ether and the crystal was fixed on top of a Kapton micro sampler, transferred to the diffractometer and frozen under a stream of cold nitrogen. A matrix scan was used to determine the initial lattice parameters. Reflections were merging and correction for Lorentz and polarisation effects, scan speed and background using SAINT.⁴⁰ Absorption corrections, including odd and even ordered spherical harmonics were performed using SADABS.⁴⁰ Based on systematic absences, E-statistics, successful refinement of the structures, the space group was assigned. The structure was solved by direct methods with aid of successive difference Fourier maps, refined using APEX III software, in conjugation with SHELXL-2014/5 and SHELXL.^{41–43} Hydrogen atoms were calculated in ideal positions with $U_{iso}(H) = 1.2 U_{eq}(C)$. Non-hydrogen atoms were refined with anisotropic displacement parameters. Full-matrix least-squares refinements were carried out by minimising $\sum w(F_o^2 - F_c^2)^2$ with the SHELXL weighting scheme.⁴⁰ Neutral atom scattering factors for all atoms and anomalous dispersion corrections for the non-hydrogen atoms were taken from *International Tables for Crystallography*.⁴⁴ The unit cell contained several disordered solvent molecules (dimethyl formamide, acetone, diethyl ether), which were treated as a diffuse contribution to the overall scattering without specific atom positions using the PLATON/SQUEEZE procedure.⁴⁵ Images of the crystal structure were generated with MERCURY and PLATON.^{46,47} CCDC 2143205 contains the supplementary crystallographic data for this paper (see also SI). This data is provided free of charge by The Cambridge Crystallographic Data Centre.

Electrostatic potential analysis

The quantum-chemical calculation was performed using the software package *GAUSSIAN 16.B.01*. Single point calculation using the geometry derived by the crystal structure data were performed using hybrid functional B3LYP^{48–50} in combination with an Alrich def2 basis set with single- ζ valence split (SVP).^{51,52} The program *MultiWfn 3.8*⁵³ was used for surface analysis. For the calculation of the electrostatic potential the grid spacing was set to 0.2 Bohr resulting in sufficiently accurate results (see Figure S26). The *van der Waals* surface is referred to as the isosurface of $q = 0.001$ e/bohr³.⁵⁴ *VMD 1.9.1*⁵⁵ was used for the visualisation and analysis of the electrostatic potential.

Quantum Yield Determination

Quantum yield of fluorescence was calculated by comparison to a reference standard (Rhodamine 6G in degassed ethanol, $\phi =$

94% at room temperature). UV-Visible absorption spectra were recorded on a Cary 60 UV-Vis spectrometer (Agilent Technologies). Emission spectra were recorded on a Cary Eclipse Fluorescence Spectrophotometer (Agilent Technologies). The selected fluorophore was dissolved in degassed DMSO to a concentration corresponding to UV-Visible absorbance 0.8 A.U. *ca.* ($\lambda_{(max)} = 523 - 535$ nm; 25 °C). The solution was transferred to a fluorescence spectrophotometer and an emission spectrum was recorded (excitation wavelength 595 nm).

Stability studies by UV-Visible Spectroscopy

To investigate the stability of the metallacages in solution, UV-Visible absorption spectra were recorded on a Cary 60 UV-Vis spectrometer (Agilent Technologies). For each compound, stock solutions at a concentration of $3 \cdot 10^{-3}$ M were prepared. An aliquot was diluted either with 1x PBS (pH 7.4) or deionised water and the UV-Vis spectra measured at different times immediately after dilution at room temperature over 24 h. The cuvette was then shaken and another spectrum recorded, to determine if the compound was altered during the 24 h or if the reduction in absorption was only due to precipitation.

Cisplatin encapsulation studies

Each metallacage (*ca.* 8 mg, 1.00 eq.) was dissolved in 0.5 mL DMF-*d*₇ and a ¹H NMR spectrum was recorded. Afterwards, cisplatin (2.00 eq.) was added to the NMR tube and the deuterated solution was stirred for 10 min before the ¹H NMR spectrum was recorded. Finally, NMR spectra were compared to evaluate any chemical shifts due to the encapsulation of cisplatin. Both spectra were calibrated to the residual solvent signal of the carbonyl proton of DMF (8.03 ppm).

Glutathione stability studies

Cages **C1.BF₄** or **C2.BF₄** were dissolved in a 9:1 ratio of DMSO-*d*₆:D₂O (0.5 mL) and a ¹H NMR spectrum was recorded. L-glutathione was added to the solution to achieve a final concentration of 2 mM (GSH : cage ratio = 1: 1) and the first ¹H NMR spectrum was immediately recorded. Afterwards, spectra were recorded every 5 min for the first hour, and every hour for the following 17 hours. Finally, an excess of L-glutathione (up to 4 mM) was added after 18 h.

Cell culture maintenance

Three human cell lines were used in the experiments. Malignant melanoma (A375), breast carcinoma molecular subtype Luminal A (MCF-7) and breast carcinoma subtype Her2+ (SK-BR-3) were obtained from ATCC. All cell lines were maintained in culture according to provider instructions and cultured in a humidified atmosphere at 37 °C and 5% CO₂. A375 and SK-BR-3 were cultured in DMEM Dulbecco's Modified Eagle Medium (DMEM, 4.5 g/L glucose, Corning, Thermo Fischer Scientific) supplemented with 10% Fetal Bovine Serum (FBS, Eu-approved South American Origin, Thermo Fisher Scientific) and 1% penicillin/streptomycin (Gibco), herein referred to as complete medium, and passaged when reaching confluence. MCF-7 was grown in Roswell Park Memorial Institute (RPMI, L-glutamine,

Corning) medium, supplemented with 10% FBS and 1% penicillin/streptomycin, and appropriately passage diluted upon reaching confluence. All cells were subjected to routine mycoplasma testing.

Antiproliferative assays

To evaluate the antiproliferative effect of the compounds the cell lines, 96-well tissue culture-treated black plates (Cellstar®, Greiner Bio-one) were seeded in a concentration of 15000 cells/well for A375 and 10000 cells/well for MCF-7 and SK-BR-3 with 200 µL full medium. Working solutions of ligand and cage samples were prepared in the required concentration by diluting fresh stock solutions (5 mM in DMSO) of the corresponding compound in aqueous complete DMEM or RPMI medium accordingly. Solutions (1 mM stock) of cisplatin were freshly prepared in aqueous solution and mixed with the metallacages prior each experiment. Cage formation and cisplatin encapsulation were confirmed by ¹H NMR spectroscopy as previously reported.^{29,56,57} Following the initial 24 h incubation required for cell adhesion, cells were incubated for an additional 24 h with 200 µL of the compounds' dilution in full medium per well. Afterwards, 20 µL/well of CellTiter-Blue® reagent was added to the assay plate, shaken 10 sec and incubated for 4 h at 37 °C and 5% CO₂. Fluorescent intensity (531_{Ex}/595_{Em} nm) from each well was quantified in quadruplicates for each experiment using a multi-well plate reader (VICTOR X5, Perking Elmer). The percentage of surviving cells was calculated, using GraphPad Prism software, from the ratio of fluorescence intensity of treated to untreated cells, corrected for the interfering fluorescence of the BODIPY. The EC₅₀ value for each compound was calculated as the concentration showing 50% decrease in cell growth, when compared to controls, using a nonlinear fitting of [concentration] vs response. Data is presented as mean ± SEM of at least three independent experiments.

Microscopy

Epifluorescence Microscopy

For widefield imaging, a Zeiss Axio Vert.A1 epifluorescent microscope was used. Two LD A-Plan objectives were used (20x/0.35 Ph1 and 40x/0.55 Ph1). Samples were excited with a LED fluorescence module equipped with filter cube for UV (385 nm), Blue (475 nm), Green (555 nm) and Red (630 nm). Images captured with AxioCam MRm (Zeiss).

Confocal Microscopy

For confocal imaging, a Leica SP5 confocal laser-scanning microscope equipped with a HCX PL APO 63x 1.4 NA oil immersion objective utilizing Leica Type F immersion oil. Fluorophores were excited using 405 Blue Diode (excitation wavelength 405 nm, laser intensity 30%) for DAPI and Hoechst 33342, Argon-514nm for the complexes, Argon-488nm for Dextran Alexa Fluor® 488 (Dex488) and finally HeNe-633nm for imaging of Dextran Alexa Fluor® 647 (Dex647), CellMask™ Deep Red and Cy5™. All Argon laser intensities were set at 30%. Images were captured sequentially to avoid fluorescence channel bleed-through. Acquisition of XY format was 1024 x

1024 pixels at speed of 200 Hz for fixed cells and 400-700 Hz for live cells, with a zoom factor of 1.73 producing a pixel size below the resolution limit of the microscope. Live cell images subjected to phase correction of -33.5 and Line average = 2, frame average = 1. Whole cell Z-acquisition was conducted 0.3 µm from bottom of imaging dish or well with steps of 0.5 µm (objective step limited to > 236 nm). Single slice images were taken ~ 1.5 µm above coverslip. Acquisition was kept under 1 min to avoid bleaching of the sample unless otherwise stated.

Fixed cells studies

Round glass coverslips (Ø 13mm, VWR) sterilised by UV-light were inserted in 24-well tissue culture- treated plates (Corning). A375 cells were seeded at a concentration of 50.000 cells/well and incubated at 37 °C under humidified atmosphere with 5% CO₂ for 48 h. The medium was discarded and fresh complete medium containing 5 µM of either cage or ligand was added. Following 2 h of incubation at 37 °C under tissue culture conditions or at 4 °C in the fridge, respectively, for energy requiring or independent uptake analysis, the glass coverslips were removed from the wells, washed 4x with 1x Phosphate Buffered Saline (PBS, Corning) and fixed with 4% formaldehyde (Alfa-Aesar) for 20 min at r.t. The coverslips were washed 3x with PBS and incubated for 1 min with 40 µL 1:1000 from a 1 mg/mL stock solution of 4',6-Diamidino-2-phenylindole dihydrochloride (DAPI, Sigma-Aldrich/ MERCK) at r.t.. After washing the coverslips thrice with PBS they were mounted on glass microscope slides (VWR) using Mowiol® 4-88 (Sigma-Aldrich). Fluorescence images obtained using either a Zeiss Axio Vert.A1 epifluorescent microscope or a Leica SP5 confocal laser-scanning microscope.

Immunofluorescence early endosome labelling with EEA1

Round glass coverslips (Ø 13mm, VWR) sterilised by UV-light were inserted in 24-well tissue culture- treated plates (Corning). Cells (MCF-7 and A375) were seeded at a concentration of 50.000 cells/well and incubated at 37 °C under humidified atmosphere with 5% CO₂ for 48 h. The medium was discarded and fresh medium containing 5 µM of either cage or ligand was added. Following 1 or 2 h of incubation at 37 °C under tissue culture conditions, the glass coverslips were removed from the wells, washed 4x with PBS and fixed with 4% formaldehyde for 20 min at r.t.. The coverslips were washed 3x with PBS, blocked with 50 mM ammonium chloride for 10 min at r.t. and permeabilised for 5 min at r.t. with 200 µL of a mixture containing 0.2% Triton X-100 (Acros Organics) and 2% bovine serum albumin in PBS. Following a blocking of 1 h with 150 µL of 2% FBS / 2% BSA in PBS, coverslips were incubated with 40 µL 1:200 goat anti-human EEA1 antibody (SC-6415, Santa Cruz) for 1 h at r.t. After a wash with 0.05% Triton X-100 in PBS (5 min at r.t. twice) and PBS, staining with primary antibody was followed by 1 h incubation with 40 µL mouse anti-goat antibody Cy5™ protected by direct light. Coverslips were washed again with 0.05% Triton X-100 in 1x PBS (5 min at r.t. twice) and PBS before incubation for 1 min with 40 µL 1:1000 from a 1 mg/mL stock solution of DAPI at r.t.. After washing the coverslips thrice with PBS and once with H₂O, they were mounted on glass

microscope slides using Mowiol® 4-88. Fluorescence images obtained with Leica SP5.

Live cell imaging

Imaging dish cell culture preparation

Imaging dishes of 35 mm polystyrene (PS) (MatTek) with central cover glass area (\varnothing 18 mm) were seeded at a concentration of 70.000 cells/dish and incubated at 37 °C under humidified atmosphere with 5% CO₂ for 48 h. The medium was discarded and fresh medium containing 5 μ M of either cage or ligand was added using A375, or 10 μ M cage in the case of SK-BR-3. Following 2 h of incubation at 37 °C under tissue culture conditions unless otherwise indicated, medium containing treatment was removed, and cells were washed four-fold and imaged in phenol red free DMEM medium. All live cell images were obtained using a Leica SP5 confocal laser-scanning microscope.

Uptake time lapse

After seeding A375 cells at a concentration of 70.000 cells per imaging dish for 48 h under humidified atmosphere with 5% CO₂, cells were washed fourfold with phenol red free DMEM. A closed thermostatic chamber at 37 C under 5% CO₂ atmosphere was set up for live cell imaging. The medium was discarded and fresh complete medium containing 5 μ M of **CG1.NO₃** was added. Following image stabilisation, a “xyt” image was taken with 30s-time interval of 512 x 512, with 700Hz speed and zoom of 2.5 on a Leica SP5. Focus drift correction was manual during acquisition to counter axial displacement.

Captured images were analysed after acquisition using ImageJ.²¹ Pixels above ImageJ threshold “Otsu” were determined as fluorescent (Figure S27 in the SI). Regions of interest were selected with an average area of 500 pixels representing intracellular and extracellular locations. The mean background fluorescent intensity was subsequently subtracted from the mean intracellular fluorescent intensity per time point, giving the corrected intensity value (Figure S28 in the SI).

Plasma membrane staining

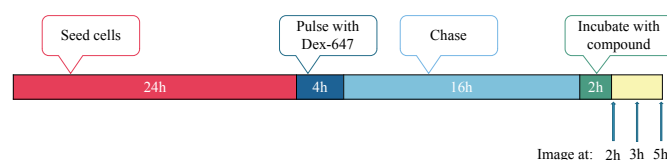
A mixture of 1 μ M Hoechst 33342 and 1 μ g/mL CellMask™ Deep Red Plasma Membrane Stain (C10046, Invitrogen) was added to A375 cells following steps described in the section on cell culture preparation above. After 5 min, cells were washed twice with phenol red free medium and imaged.

Late endosome / Lysosomal colocalisation Dextran

Imaging dishes of 35 mm polystyrene (PS) (MatTek) with central cover glass area (\varnothing 18 mm) were seeded at a concentration of 70.000 A375 cells/dish and incubated at 37 °C under humidified atmosphere with 5% CO₂ for 24 h. After, medium was discarded and lysosomes were labelled with a 4 h pulse of 200 μ g/mL Dex-647 (10.000 mol. wt. Fisher Scientific) in fresh DMEM. The Dex-647 was allowed to chase for 16 h in dextran-free medium. The medium was discarded, and cells were incubated for 2 h with fresh medium containing 5 μ M of treatment (**CG1.NO₃**, **CG1.BF₄** or **LG1**) or 200 μ g/mL Dex-488 (10.000 mol. wt. Fisher Scientific) as control at 37°C (5% CO₂). Cells were then washed with

phenol-red free medium and imaged at 2 h and re-imaged at 3 h and 5 h. For each timepoint, five images were taken. In between imaging, cells were kept at 37 °C humidified atmosphere (5% CO₂). Figure 15 illustrates the timeline of the assay. Image analysis was performed using ImageJ.⁴⁵¹ For each timepoint, “Otsu” threshold was determined from brightest image and applied as mask for the other four images. Pearsons correlation coefficient (PCC) and Manders coefficients (MC) were determined and averaged with standard deviation.

Figure 15 - Timeline of colocalisation assay.



Conclusions

In conclusion, we report here the synthesis and characterisation of two new self-assembled [Pd₂L₄]⁴⁺ cages *exo*-functionalised with BODIPY moieties, endowed with excellent luminescent properties and featuring a hydrophobic cavity able to encapsulate the anticancer drug cisplatin. The 3,5-bis(3-ethynylpyridine)phenyl ligands differ for one CH₂ group between the ligand scaffold and the BODIPY moiety anchored via amide bond. The cage with the shorter linkage features high quantum yield and sufficient stability in buffered solution, including in the presence of physiologically relevant concentration of GSH. With the aim of understanding the fate of metallacages in cancer cells, fluorescence microscopy was used on fixated and live cells. In melanoma A375 cells, cage **CG1** is efficiently taken up via active transport mechanisms in the first hours and rapidly accumulates in sub-cellular vesicular structures, likely to correspond to melanosomes. Preliminary immunolabeling of endosomal markers show that there is little evidence that the cage has entered the canonical EEA1 labelled early endosome. The possibility exists that it may enter via a different pathway that does not lead to accumulation in the lysosome. Further analysis will reveal whether this observation is specific to melanoma cells, as the breast cancer cell line SK-BR-3 provided a very different subcellular profile. Here, **CG1** was observed to be localised throughout the cytoplasm in reticular-like structures with also some evidence of vesicular localisation. Surprisingly, no evidence of **CG1** uptake was observed in MCF-7 cells. The obtained results may account for the obtained antiproliferative effects of the [(cisplatin)₂CG1] host-guest complex, featuring an enhanced activity only against SK-BR-3 cells in comparison to free cisplatin. In fact, we hypothesize that only when the cage and its cargo are not subjected to sequestration in sub-cellular compartments, as observed in A375 and SK-BR-3 cells, the supramolecular complex exerts its drug transporting function. Future studies with BODIPY-functionalised [Pd₂L₄]⁴⁺ cages could also be explored for photodynamic therapy. For example, a highly emissive Pt²⁺ supramolecular triangle bearing a pyridine-functionalized BODIPY ligand was reported, whereby the BODIPY was synergistically acting as imaging probe and photo-sensitiser.²⁸

While further studies are necessary to validate 3-dimensional metallacages as novel drug delivery systems and *theranostic* agents, the obtained results shed further light into the development of supramolecular coordination complexes for biomedical applications.

Author Contributions

B.A. performed the antiproliferative activity tests and the fluorescence microscopy studies, as well as the related data analysis. R.B., B.W., D.D. and R.S. performed the synthesis and characterisation of the reported ligands and cage compounds; D.D. optimised the synthesis of one of the BODIPY fluorophores. R.B. and D.D. performed the UV-Vis and NMR spectroscopy studies. E.J.S. supervised the fluorescence microscopy studies and the data analysis. C.S. performed the synthesis of cage [Pd₂L₂]⁴⁺ and its crystallisation studies; A.A.H. and A.P. performed the XRD and electrostatic surface potential analysis. A.C. and A.J. were responsible for the project conceptualisation, supervision, data analysis, writing of the original draft and funding acquisition. All authors contributed to writing part of the results section and revised the manuscript before submission.

Conflicts of interest

There are no conflicts to declare.

Acknowledgements

We thank Christian Jandl (Department of Chemistry, TUM) for the SC-XRD measurement of cage [Pd₂L₂]⁴⁺. Support from TUM Innovation Network Artificial Intelligence in Material Science (ARTEMIS) is gratefully acknowledged.

References

- 1 K. Hemmer, M. Cokoja and R. A. Fischer, *ChemCatChem*, 2021, **13**, 1683.
- 2 A. Schneemann, V. Bon, I. Schwedler, I. Senkovska, S. Kaskel and R. A. Fischer, *Chem. Soc. Rev.*, 2014, **43**, 6062.
- 3 H.-C. Zhou, J. R. Long and O. M. Yaghi, *Chem. Rev.*, 2012, **112**, 673.
- 4 R. Chakrabarty, P. S. Mukherjee and P. J. Stang, *Chem. Rev.*, 2011, **111**, 6810.
- 5 A. Pöthig and A. Casini, *Theranostics*, 2019, **9**, 3150.
- 6 G. Yu, M. Jiang, F. Huang and X. Chen, *Curr. Opin. Chem. Biol.*, 2021, **61**, 19.
- 7 H. Sepehrpour, W. Fu, Y. Sun and P. J. Stang, *J. Am. Chem. Soc.*, 2019, **141**, 14005.
- 8 Z. Yue, H. Wang, Y. Li, Y. Qin, L. Xu, D. J. Bowers, M. Gangoda, X. Li, H.-B. Yang and Y.-R. Zheng, *Chem. Commun.*, 2018, **54**, 731.
- 9 O. Domarco, D. Lötsch, J. Schreiber, C. Dinhof, S. Van Schoonhoven, M. D. García, C. Peinador, B. K. Keppler, W. Berger and A. Terenzi, *Dalt. Trans.*, 2017, **46**, 329.
- 10 S. F. J. B. NP, J.-J. L. S.-F. G and T. B. J. *Am. Chem. Soc.*, 2012, **134**, 754.
- 11 J. Xu, J. Wang, J. Ye, J. Jiao, Z. Liu, C. Zhao, B. Li and Y. Fu, *Adv. Sci.*, 2021, **8**, 2101101.
- 12 M. D. Ward, C. A. Hunter and N. H. Williams, *Acc. Chem. Res.*, 2018, **51**, 2073.
- 13 D. A. J. Metherell, D. W. Cullen, P. N. H. Williams and P. M. D. Ward, *Chem. – A Eur. J.*, 2018, **24**, 1554.
- 14 D. K. Chand, K. Biradha and M. Fujita, *Chem. Commun.*, 2001, **1**, 1652.
- 15 J. E. M. Lewis, E. L. Gavey, S. A. Cameron and J. D. Crowley, *Chem. Sci.*, 2012, **3**, 778.
- 16 D. Preston, A. Fox-Charles, W. K. C. Lo and J. D. Crowley, *Chem. Commun.*, 2015, **51**, 9042.
- 17 A. Schmidt, V. Molano, M. Hollering, A. Pöthig, A. Casini and F. E. Kühn, *Chem. – A Eur. J.*, 2016, **22**, 2253.
- 18 A. Schmidt, M. Hollering, M. Drees, A. Casini and F. E. Kühn, *Dalt. Trans.*, 2016, **45**, 8556.
- 19 A. Schmidt, M. Hollering, J. Han, A. Casini and F. E. Kühn, *Dalt. Trans.*, 2016, **45**, 12297.
- 20 J. Han, A. Schmidt, T. Zhang, H. Permentier, G. M. M. Groothuis, R. Bischoff, F. E. Kühn, P. Horvatovich and A. Casini, *Chem. Commun.*, 2017, **53**, 1405.
- 21 J. Han, A. F. B. Räder, F. Reichart, B. Aikman, M. N. Wenzel, B. Woods, M. Weinmüller, B. S. Ludwig, S. Stürup, G. M. M. Groothuis, H. P. Permentier, R. Bischoff, H. Kessler, P. Horvatovich and A. Casini, *Bioconjug. Chem.*, 2018, **29**, 3856.
- 22 B. Woods, R. D. M. Silva, C. Schmidt, D. Wragg, M. Cavaco, V. Neves, V. F. C. Ferreira, L. Gano, T. S. Morais, F. Mendes, J. D. G. Correia and A. Casini, *Bioconjug. Chem.*, 2021, **32**, 1399.
- 23 F. Kaiser, A. Schmidt, W. Heydenreuter, P. J. Altmann, A. Casini, S. A. Sieber and F. E. Kühn, *Eur. J. Inorg. Chem.*, 2016, **2016**, 5189.
- 24 B. Woods, D. Döllerer, B. Aikman, M. N. Wenzel, E. Sayers, F. E. Kühn, A. Jones and A. Casini, *J. Inorg. Biochem.*, 2019, **199**, 110781.
- 25 E. Martinou, K. Seintis, N. Karakostas, A. Bletsou, N. S. Thomaidis, M. Fakis and G. Pistolis, *J. Phys. Chem. C*, 2017, **121**, 5341.
- 26 G. Gupta, A. Das, K. C. Park, A. Tron, H. Kim, J. Mun, N. Mandal, K.-W. Chi and C. Y. Lee, *Inorg. Chem.*, 2017, **56**, 4615.
- 27 G. Gupta, A. Das, S. Panja, J. Y. Ryu, J. Lee, N. Mandal and C. Y. Lee, *Chem. – A Eur. J.*, 2017, **23**, 17199.
- 28 J. Zhou, Y. Zhang, G. Yu, M. Crowley, C. Fulong, A. Friedman, S. Sengupta, J. Sun, Q. Li, F. Huang and T. Cook, *J. Am. Chem. Soc.*, 2018, **140**, 7730.
- 29 B. Woods, M. N. Wenzel, T. Williams, S. R. Thomas, R. L. Jenkins and A. Casini, *Front. Chem.*, 2019, **0**, 68.
- 30 A. Ahmedova, R. Mihaylova, D. Momekova, P. Shestakova, S. Stoykova, J. Zaharieva, M. Yamashina, G. Momekov, M. Akita and M. Yoshizawa, *Dalt. Trans.*, 2016, **45**, 13214.
- 31 D. Montero, C. Tachibana, J. Rahr Winther and C. Appenzeller-Herzog, *Redox Biol.*, 2013, **1**, 508.
- 32 J. M. Wilson, M. De Hoop, N. Zorzi, B. H. Toh, C. G. Dotti and R. G. Parton, *Mol. Biol. Cell*, 2000, **11**, 2657.
- 33 P. R. Moody, E. J. Sayers, J. P. Magnusson, C. Alexander, P. Borri, P. Watson and A. T. Jones, *Mol. Ther.*, 2015, **23**, 1888.
- 34 F. T. Mu, J. M. Callaghan, O. Steele-Mortimer, H. Stenmark, R. G. Parton, P. L. Campbell, J. McCluskey, J. P. Yeo, E. P. C. Tock and B. H. Toh, *J. Biol. Chem.*, 1995, **270**, 13503.
- 35 R. Kametseva, V. Kosheverova, M. Kharchenko, M. Zlobina, A. Salova, T. Belyaeva, N. Nikolsky and E. Kornilova, *PLoS One*, 2020, **15**, e0232532.
- 36 X. Y. Liu, H. Fang, Z. G. Yang, X. Y. Wang, L. M. Ruan, D. R. Fang, Y. G. Ding, Y. N. Wang, Y. Zhang, X. L. Jiang and H. C. Chen, *Int. J. Dermatol.*, 2008, **47**, 448.
- 37 F. P. Cordeli, S. Bolte and Jac. v2. 0. improving the user experience with co-localization Studies, 2008.
- 38 G. Raposo and M. S. Marks, *Nat. Rev. Mol. Cell Biol.* 2007 **8**10, 2007, **8**, 786.
- 39 APEX, suite of crystallographic software, APEX3, Version 2015-5.2, Bruker AXS Inc., Madison, Wisconsin, USA, 2015.
- 40 SAINT, Version 8.40A and SADABS, Version 2016/2, Bruker AXS Inc., Madison, Wisconsin, USA, 2016.

- 41 G. M. Sheldrick, *Acta Crystallogr. Sect. A Found. Crystallogr.*, 2015, **71**, 3.
- 42 G. M. Sheldrick, *Acta Crystallogr. Sect. C Struct. Chem.*, 2015, **71**, 3.
- 43 C. B. Hübschle, G. M. Sheldrick and B. Dittrich, *J. Appl. Crystallogr.*, 2011, **44**, 1281.
- 44 *International Tables for Crystallography*, Vol. C (Ed.: A. J. Wilson), Kluwer Academic Publishers, Dordrecht, The Netherlands, 1992, Tables 6.1.1.4 (pp. 500–502), 4.2.6.8 (pp. 219–222), and 4.2.4.2 (pp. 193–199).
- 45 A. L. Spek, *Acta Crystallogr. Sect. C, Struct. Chem.*, 2015, **71**, 9.
- 46 C. F. Macrae, I. J. Bruno, J. A. Chisholm, P. R. Edgington, P. McCabe, E. Pidcock, L. Rodriguez-Monge, R. Taylor, J. Van De Streek and P. A. Wood, *J. Appl. Crystallogr.*, 2008, **41**, 466.
- 47 A. L. Spek, *Acta Crystallogr. Sect. D Biol. Crystallogr.*, 2009, **65**, 148.
- 48 P. J. Stephens, F. J. Devlin, C. F. Chabalowski and M. J. Frisch, *J. Phys. Chem.*, 1994, **98**, 11623.
- 49 A. D. Becke, *J. Chem. Phys.*, 1993, **98**, 5648.
- 50 C. Lee, W. Yang and R. G. Parr, *Phys. Rev. B*, 1988, **37**, 785.
- 51 A. Schäfer, C. Huber and R. Ahlrichs, *J. Chem. Phys.*, 1994, **100**, 5829.
- 52 A. Schäfer, H. Horn and R. Ahlrichs, *J. Chem. Phys.*, 1992, **97**, 2571.
- 53 T. Lu and F. Chen, *J. Comput. Chem.*, 2012, **33**, 580.
- 54 R. F. W. Bader, M. T. Carroll, J. R. Cheeseman and C. Chang, *J. Am. Chem. Soc.*, 1987, **109**, 7968.
- 55 W. Humphrey, A. Dalke and K. Schulten, *J. Mol. Graph.*, 1996, **14**, 33.
- 56 H. Song, S. Rajendiran, N. Kim, S. K. Jeong, E. Koo, G. Park, T. D. Thangadurai and S. Yoon, *Tetrahedron Lett.*, 2012, **53**, 4913.
- 57 M. Yu, J. K.-H. Wong, C. Tang, P. Turner, M. H. Todd and P. J. Rutledge, *Beilstein J. Org. Chem.* **116**, 2015, **11**, 37.